Recent progress in the assessment of irradiation effects for in-vessel fusion materials: tungsten and copper alloys

D. Terentyev[1,*], M. Rieth[2] , G. Pintsuk[3] , J. Riesch[4], A. von Müller[5],
S. Antusch[2], K. Mergia[4] , E. Gaganidze[2], H.-C. Schneider[2], M. Wirtz[3] ,
S. Nogami[6], J. Coenen[3], J.H. You[5], A. Zinovev[1] and W. Van Renterghem[1]

[1] Belgian Nuclear Research Centre, SCK●CEN, Mol, 2400, Belgium
[2] Karlsruhe Institut für Technologie, Hermann-von-Helmholtz-Platz 1, 76344 Eggenstein-Leopoldshafen, Germany
[3] Forschungszentrum Jülich GmbH, Institut für Energie- und Klimaforschung – Plasmaphysik, 52425 Jülich, Germany
[4] NCSR Demokritos, Institute of Nuclear and Radiological Science and Techology, Energy and Safety, 15310 Agia Paraskevi, Greece
[5] Max-Planck-Institut für Plasmaphysik, 85748 Garching, Germany
[6] Tohoku University, 6-6-01-2, Aramaki-aza-Aoba, Aoba-ku, Sendai, 980-8579, Japan

E-mail: dmitry.terentyev@sckcen.be

Abstract

The present contribution highlights results of the recent irradiation campaigns applied to screen mechanical properties of advanced tungsten and copper-based materials—main candidates for the application in the plasma-facing components (PFC) in the European DEMO, which has also been presented at 28th IAEA fusion energy conference. The main challenges in the formulated irradiation programme were linked to: (I) assessment of the ductile-to-brittle transition temperature of newly developed tungsten-based materials; (ii) investigation of an industrial pure tungsten grade under high temperature irradiation, reflecting operational conditions in the high flux divertor region; (iii) assessment of the high temperature strength of CuCrZr-based alloys and composites developed to enable the extension of the operational window for the heat sink materials. The development and choice of the advanced materials is driven naturally by the need to extend the operation temperature/fluence window thereby enlarging the design space for PFCs. The obtained results helped identifying the prospective tungsten and copper-based material grades as well as yielded a number of unexpected results pointing at severe degradation of the mechanical properties due to the irradiation. The results are discussed along with the highlights of the microstructural examination. An outlook for near future investigations involving in-depth post-irradiation examination and further irradiation campaigns is provided.

Keywords: irradiation, plasma facing materials, embrittlement, hardening

(Some figures may appear in colour only in the online journal)

1. Introduction

DEMO and fusion power plants beyond it require robust materials to ensure durable and safe operation as well as commercially competitive construction and dismantling design. One of the main challenges in the development of those materials is the assessment of irradiation effects, originating from the nuclear fusion reaction, which generates 14 MeV neutrons damaging the materials atomic lattice. So called in-vessel materials will experience the most severe neutron exposure being far beyond the damage limits acquired by currently operating nuclear power plants. The development of high temperature irradiation resistant materials with superior mechanical properties is critical for the enhancement of the operational lifetime of reactor components and thus important for end goal—cost efficiency. As a matter of fact, there is already a number of examples in literature demonstrating the advance achieved e.g. in tungsten (see e.g. [1–9]). The development of the advanced tungsten materials followed a general route for the development of nuclear materials (mostly steels) where a combination of heat/mechanical/chemical treatment is applied to improve specific property(ies) without compromising baseline performance. One specific milestone to be achieved in this development cycle is the validation of the material performance under high flux of fast neutrons which would mimic the irradiation field of the nuclear fusion reactor. The present contribution specifically addressed this step and highlights the results presented at the recently held 28th Fusion Energy Conference organized by IAEA.

In general, the task of the development and qualification of the in-vessel materials boils down to securing that the degradation of mechanical, thermal and physical properties will remain within acceptable limits, which are in turn driven by the design of components and operational scenario. Overall, three main functions of the in-vessel materials can be singled out, such as: structural (steel), armour (tungsten) and heat sink (copper). For some materials the function can be mixed, i.e. heat sink and structural for the copper pipe.

The assessment of the irradiation effects in candidate DEMO in-vessel materials is one of the priorities within European materials programme [10]. This contribution highlights the recent efforts made for the armour and heat sink materials, in particular for the application in the high flux divertor region. Based on the already available knowledge (see e.g. [11–14] and references cited therein), the operational conditions for the baseline tungsten and copper materials are tentatively determined as illustrated on figure 1. For each of the baseline materials, the lower temperature bound is defined by the embrittlement (fracture without plastic deformation), while the upper temperature bound is determined by the softening of the material (reduction of the yield point). Accordingly, the main challenges in the formulated irradiation programmes were linked to: (I) assessment of the ductile-to-brittle transition temperature (DBTT) of baseline tungsten and advanced tungsten composites; (ii) investigation of baseline tungsten under irradiation at very high temperature, reflecting operational conditions in the high flux divertor region; (iii) assessment of the mechanical properties of CuCrZr-based alloys and

composites. The choice of the advanced materials is driven naturally by the need to extend the operation temperature/fluence window in order to extend the design space. Here, we present the most recent results obtained for a number of tungsten and copper-based alloys identified thanks to down-selection on the basis of preliminary tests so far not involving neutron irradiation.

The neutron exposure was realized in the Belgian material test reactor (BR2), and the irradiation capsules were placed directly inside the fuel elements to minimize the generation rate of Re/Os transmutation due to thermal neutrons, thus approaching fusion relevant conditions with a high energy neutron spectrum. The target irradiation fluence was defined as 1 dpa (in W) corresponding to the expected damage at the end-of-operation of ITER. Extraction of the properties of the neutron exposed materials involved extensive post irradiation examination (PIE) campaigns in Germany, Belgium, and Greece.

2. Investigated materials and methodology

The basic information about the materials investigated here is summarized in table 1. More information about the fabrication route, microstructure and mechanical properties in the non-irradiated state can be found in the references provided in the table. The samples were manufactured to their final shape by the material suppliers, as specified in the table, except the reference tungsten, for which the samples were fabricated using the electric discharge machine at SCK CEN.

Neutron irradiation on the various materials and specimen shapes was performed in BR2 inside the fuel element in the position close to the center of the reactor and in the mid-plane with the average fast neutron ($E > 1$ MeV) flux of 1×10^{14} n cm^{-2} s^{-1} at a power of 60 MW. The samples were encapsulated in a steel tube with 1.5 mm wall thickness filled with He. The gap between the samples and the pressure tube was adjusted to achieve a target temperature during the irradiation following thermal and neutronic calculations. According to a finite element analysis of thermal flow, variation of 25 °C–50 °C occurred during the irradiation cycle (the lower the absolute irradiation temperature, the lower its in-cycle variation) due to the burnup of the fuel element. The irradiation dose was calculated by MCNPX 2.7.0 [15]. The dpa cross sections for W have been prepared from the JENDL4 file (MT444) for the threshold displacement energy of 55 eV, following the recommendation of IAEA [16]. The transmutation of Re and Os was calculated based on the ALEPH code developed by SCK CEN and available nuclear databases [17–21]. The typical transmutation rate from W to Re was about 1.8–2 at.% per dpa. The irradiation duration was between 143 and 201 reactor operational days depending on the position of the capsule in the reactor channel, as was assessed in our previous works [22, 23]. The irradiation dose on tungsten samples was 1.04–1.25 dpa (dpa is calculated in W), and on copper-based materials 1.02–1.25 dpa (dpa is calculated in W).

Pre-irradiation examination and PIE via mechanical tests was conducted using certified equipment in hot cells in the premises of the research centers KIT and SCK CEN in
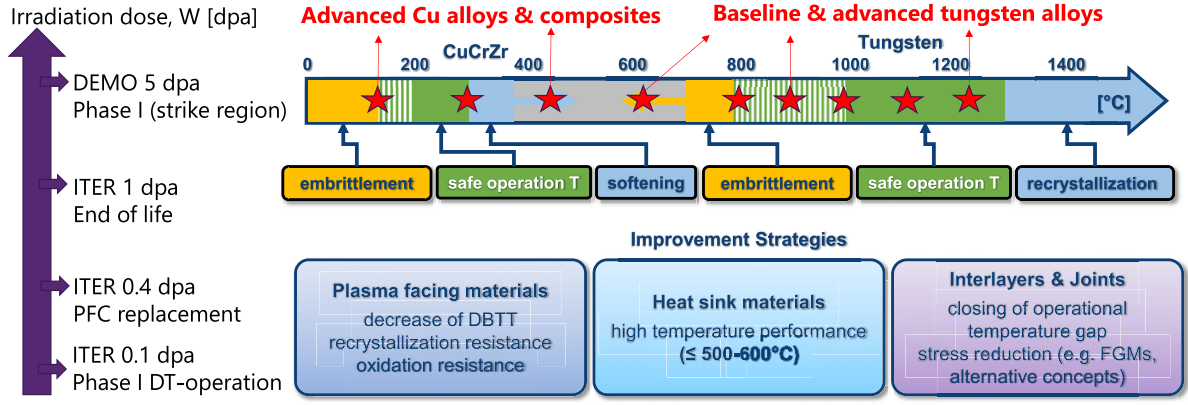
Figure 1. EU programme on irradiation testing of high heat flux materials.

Germany and Belgium, respectively. The mechanical characterization comprised fracture toughness, tensile and three-point bending tests. Due to an extensive number of required tests, the PIE programme was shared between the two labs. However, the below-described mechanical testing was performed on the accredited and duly calibrated equipment in each lab. Instron universal test bench with hydraulic actuator, 50 kN load cell and environmental chamber (reaching up to 580 °C, higher test temperature capability was not available yet) was used at SCK CEN to test both reference and as-irradiated samples. Whereas at KIT, the reference tests were performed also with Instron (100 kN load cell) equipped with a vacuum high temperature furnace from Mytec GmbH (reaching up to 1500 °C, 10^{-5} mbar), the testing of irradiated specimens was performed with servo-electric bench from Zwick GmbH (10 kN load cell) equipped with Mytec furnace (up to 1200 °C, 6×10^{-5} mbar) and installed in the Hot cells. Detailed information on the test conditions, sample geometries and test procedures can be found in [24–26]. The most essential information on the test procedures and parameters is summarized below.

Uniaxial tensile tests were performed on mini flat dog-bone shaped specimens with a length of 16 mm, a gauge length of 5.2 mm and an effective cross section of 2.4 mm^2. The strain was calculated based on the measurements of the pull rod displacement using linear variable differential transformer (LVDT). The strain rate applied was 6×10^{-4} s^{-1}. The LVDT and the load cell were calibrated according to the required standards on the equipment applied to test both irradiated and reference samples. Tests were performed according to the ASTM E8 guidelines.

Miniaturized three-point bending (3PB) specimens were tested using the configuration according to the ASTM standard E290 [27]. The span between the lower supporting pins was 8.5 mm and their diameter was 2.5 mm. The samples had dimensions $1 \times 1 \times 12$ mm^3 with a polished surface. L-T orientation was applied for the textured materials (i.e. tungsten plates and tungsten rod). The strain rate applied was

1×10^{-3} s^{-1} i.e. very close to the one applied for the tensile tests. Tensile and bending tests were performed at SCK CEN in air.

Fracture toughness measurements were performed using 3PB and disk-shaped compact tension (DCT) specimens with a narrow notch with a root radius around 50 μm cut by EDM. Fracture toughness samples were machined in the T-L orientation. The T-L orientation for the fracture toughness assessment has been selected in accordance with the texture of PFC ITER components (i.e. thermal stresses act normal to the rolling direction). The test temperature for irradiated specimens ranged from RT up to 1100 °C at KIT, and up to 580 °C at SCK CEN. The stress intensity factor rate was 0.7 MPa m$^{1/2}$ s^{-1}. K_Q values (linear elastic stress intensity factor) were calculated according to the requirements of ASTM E399 [28]. Equation (1) is used for the determination of the fracture toughness K_Q for mode I fracture:

$$K_Q = \frac{P_Q}{B\sqrt{W}} \cdot f\left(\frac{a}{W}\right), \qquad (1)$$

where P_Q is defined either as the load at fracture in case of the absence of plastic deformation or as the load at the intersection of the loading curve with the straight line exhibiting a slope that is 95% of the elastic slope in case plastic deformation occurs; $f\left(\frac{a}{W}\right)$ is a geometry dependent function related to the ratio between the crack size a and the width W, which can be found in the standard; B is the specimen thickness.

The fracture surface of the tested samples was inspected by SEM using the same methodology as earlier applied in [29]. The conclusion on the prevailing type of the microstructure was based on the detailed inspection of three to five zones for each test condition. All SEM images were acquired using a secondary electron detector, so as to effectively reveal the small features (<1 μm) on the fracture surface. The employed scanning electron microscope was a JEOL JSM-6610LV (JEOL, Tokyo, Japan) and the operating conditions were: 20 kV accelerating voltage and 10–20 mm working dis-

Table 1. Summary of information on the advanced materials. Coloumn 'reference' points to earlier works where the microstructure and mechanical properties of a corresponding material were investigated.

Material form of product supplier	Reference, ID used in paper	Advantages/selection criteria
Pure W (IGP) Forged bar, 36×36 mm cross-section Plansee AG (Austria)	[26, 30] IGP	Industrial material grade, well-established fabrication methodology, numerous experimental data available
K-doped W and K-doped W/Re (3% Re) Hot-rolled plates, $d = 7$ mm Tohoku Univ (Japan)	[6, 7] W–K (Tohoku) W–Re–K (Tohoku)	Industrial material, established fabrication methodology, engineering-relevant plate thickness is available, low DBTT. Potential tolerance to the irradiation damage thanks to fine-grain structure. Improved resistance against recrystallization
Powder injection molded W with TiC and Y_2O_3 particle reinforcement Disks/plates, $d = 4$ mm KIT (Germany)	[31] PIM W-TiC PIM W–Y_2O_3	Net-shape component production, flexibility on the micro-alloying, up-scalable fabrication methodology. Improved resistance against recrystallization
K-doped cold-rolled W Plate, $d = 1$ mm KIT (Germany)	[32] W–K (KIT)	Unique combination of ductility, strength and low DBTT. Potential tolerance to the irradiation damage thanks to fine-grain structure. resistance against recrystallization
CuCrZr–W laminates (W-27wt.% CuCrZr) Plate, $d = 1$ mm KIT (Germany)	[33, 34] CuCrZr–W_L	Unique combination of ductility, strength and low DBTT. High potential for large scale production
W fiber-reinforced CuCrZr (46 wt.%) Plate, Wf $\emptyset = 150~\mu$m, $d = 1$ mm IPP Garching (Germany)	[35–37] CuCrZr–W_f	Combination of ductile CuCrZr matrix with high-strength drawn W fibers as reinforcement
W particle-reinforced CuCrZr (70/30 wt.% W/CuCrZr) Plate, $d = 1$ mm IPP Garching (Germany)	[38] CuCrZr–W_P	Combination of ductile CuCrZr matrix with W particles as reinforcement
Copper strengthened by Y_2O_3 ODS (Y: 0.56wt.%, O: 0.32 wt.%) particles and V-added precipitates (Cu-0.922%Cr-0.041%Zr-0.221%V, wt.%). Supplied by KIT (Germany)	Cu-ODS CuCrZr–V	High temperature strength and creep resistance thanks to the precipitation strengthening

tance. The residual gamma irradiation of the samples was too high to perform reliable chemical analysis using an integrated EDS detector.

The TEM samples were investigated with a JEOL 3010 TEM operating at 300 kV. Conventional bright field and dark field diffraction contrast images were recorded mostly under weak beam two beam conditions. The orientation of the sample was determined from selected area diffraction patterns. Defect densities were obtained by counting the number of defects within a single frame and dividing it by the volume. To determine the volume, the surface area was multiplied with the local thickness, determined from convergent beam electron diffraction patterns, in the middle of the field of view. The number densities were corrected for extinction conditions, based on the results of the defect characterization. They were measured at several different locations within the sample and the average density is reported. Loop sizes were measured as the longitudinal axis of the elliptically shaped contrast. Cavities were visualized in out-of-focus imaging conditions with a defocus of about 750 nm. The sizes of the cavities were measured in the under-focus images at the border between the bright and dark fringe.
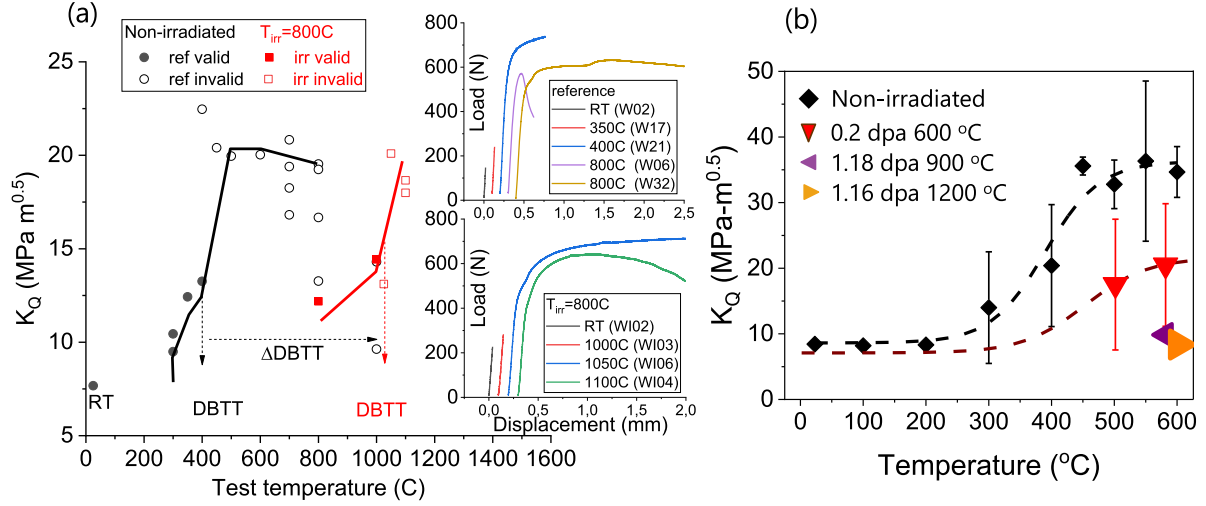
Figure 2. Assessment of the irradiation embrittlement in pure tungsten (baseline material). (*a*): the fracture toughness after irradiation at 800 °C 1.25 dpa, in-depth study is presented in [24], two inset figures show the load-displacement curves measured at different test temperatures before (upper inset) and after (lower inset) irradiation; (*b*): the fracture toughness after irradiation at 600, 900 and 1200 °C. The irradiation dose is specified on the legend of the figure.

3. Results and discussion

3.1. Tungsten-based materials

3.1.1. Baseline commercial pure tungsten. Assessment of the fracture toughness and associated irradiation embrittlement of tungsten is one critical gap in the tungsten material database and the related DEMO material property handbook under development [10]. Figure 2 summarizes the currently obtained results for pure tungsten irradiated at 600, 800, 900 and 1200 °C. The fracture toughness samples had T-L orientation with grains elongated perpendicular to the crack propagation direction. The DBTT of the non-irradiated tungsten with this grain orientation is about 400 °C. Figure 2(*a*) shows the evolution of the fracture toughness K_Q, which exhibits a steep rise near 400 °C as the load-displacement response reveals transition from pure elastic to elasto-plastic deformation, see the inset figure. The lower shelf fracture toughness is $\sim$7–10 MPa m$^{0.5}$, i.e. in the range of the values obtained for other tungsten products tested in the brittle state [39–41]. After irradiation at 800 °C, the onset of the plastic deformation shifts to 1025 °C (see invalid value of K_Q at 1025 °C, and load-displacement curves as well as in-depth discussion in reference [24]). K_Q measured at 800 °C is just slightly above 10 MPa m$^{0.5}$ implying that the material's fracture toughness is as low as the one of non-irradiated material in the lower shelf, i.e. the material is practically brittle. A set of tests performed at 500 °C–580 °C for the same material irradiated at 900 and 1200 °C has also revealed fully brittle fracture, confirming that the irradiation at high temperature provokes far non-negligible embrittlement, see figure 2(*b*). The samples irradiated to a lower dose (i.e. 0.2 dpa) were tested at 600 °C and some limited plastic deformation was registered on the force-displacement curves. Thus, from figure 2(*a*) we see that the DBTT shift after 1.25 dpa_800 °C is 625 °C, while it decreases to 200 °C at 0.2 dpa_600 °C (see figure 2(*b*)). This result demonstrates that the DBTT progressively increases with raising the irradiation

dose from 0.2 up to 1 dpa. The high temperature (>600 °C) test programmes are ongoing to deduce the DBTT shift for $T_{irr} = 900$ °C–1200 °C at 1 dpa, while the present study clearly points out that the transition will take place above 600 °C.

The progressive embrittlement while raising the irradiation dose from 0.1 to 1 dpa is fully consistent with a recent overview reported by Garrison *et al* [42], which highlights the results of joint US-Japan studies for irradiation temperatures in the range 370 °C–830 °C. The increase of the hardness (at RT) in single crystal W was measured for the gadolinium shielded (to reduce Re/Os generation by absorption of thermal neutrons) and un-shielded capsules up to $\sim$2 dpa showing that a steep increase in hardness occurs above 0.4–0.6 dpa irrespectively of the applied thermal neutron shielding. Earlier works by Hu *et al* [43] and Koyanagi *et al* [44] have suggested that this increase is to be associated with the formation of non-coherent Re–Os precipitates which were observed at 1 dpa and above at high irradiation temperature (>500 °C). However, the recent results of Garrison suggest that even with the shielding the irradiation hardening is nearly as significant as in the unshielded fission mixed spectrum. This important result requires further clarification by TEM as recent findings suggest the presence of heterogeneous microstructure exhibiting features such as grain boundary void depletion, dislocation line decoration by loops and void-precipitate percolations [45, 46].

Prior to present TEM findings of this work, let us briefly describe the features of the fracture surface. SEM images of the fracture surface are provided in figure 3 for the samples tested at 500 and 580 °C. In the non-irradiated state [25], the fracture surface of this material above 500 °C is characterized by the presence of intergranular ductile fracture and dimples. The signature of brittle intergranular fracture is seen already at 0.2 dpa_600 °C, as shown in figures 3(*a*) and (*b*), although intergranular dimples are also seen. At 1.16–1.18 dpa, the fracture surface often encounters regions featuring transgranular fracture showing the suppression of the intra-granular ductile
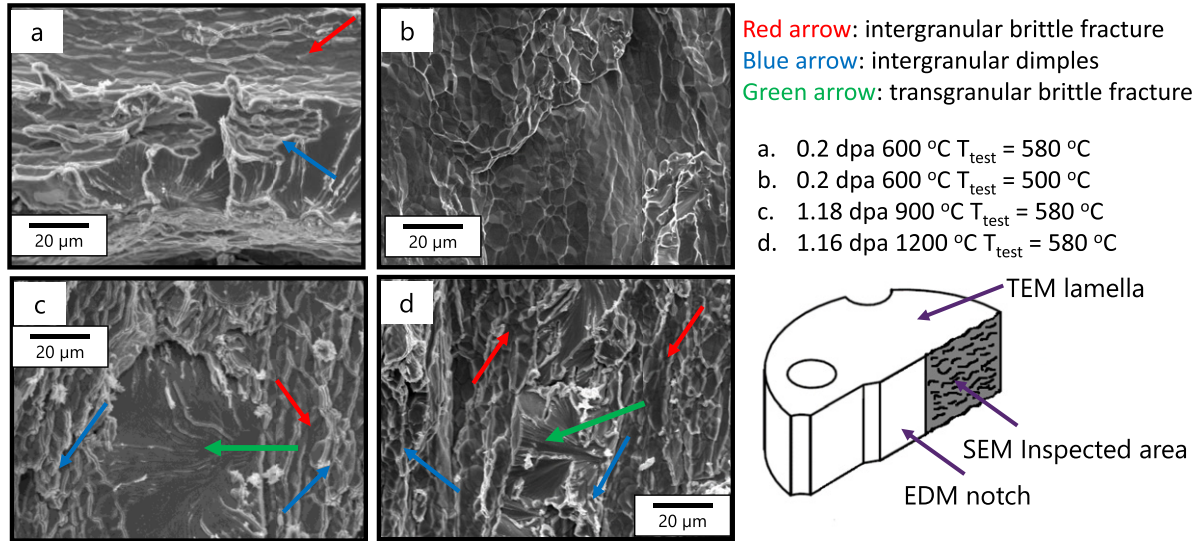
Figure 3. Examples of pure tungsten SEM images of the fracture surface taken from the fracture toughness samples. The irradiation conditions are explained on the legend. The inspected area and region for the extraction of TEM sample are shown schematically in the lower right corner.
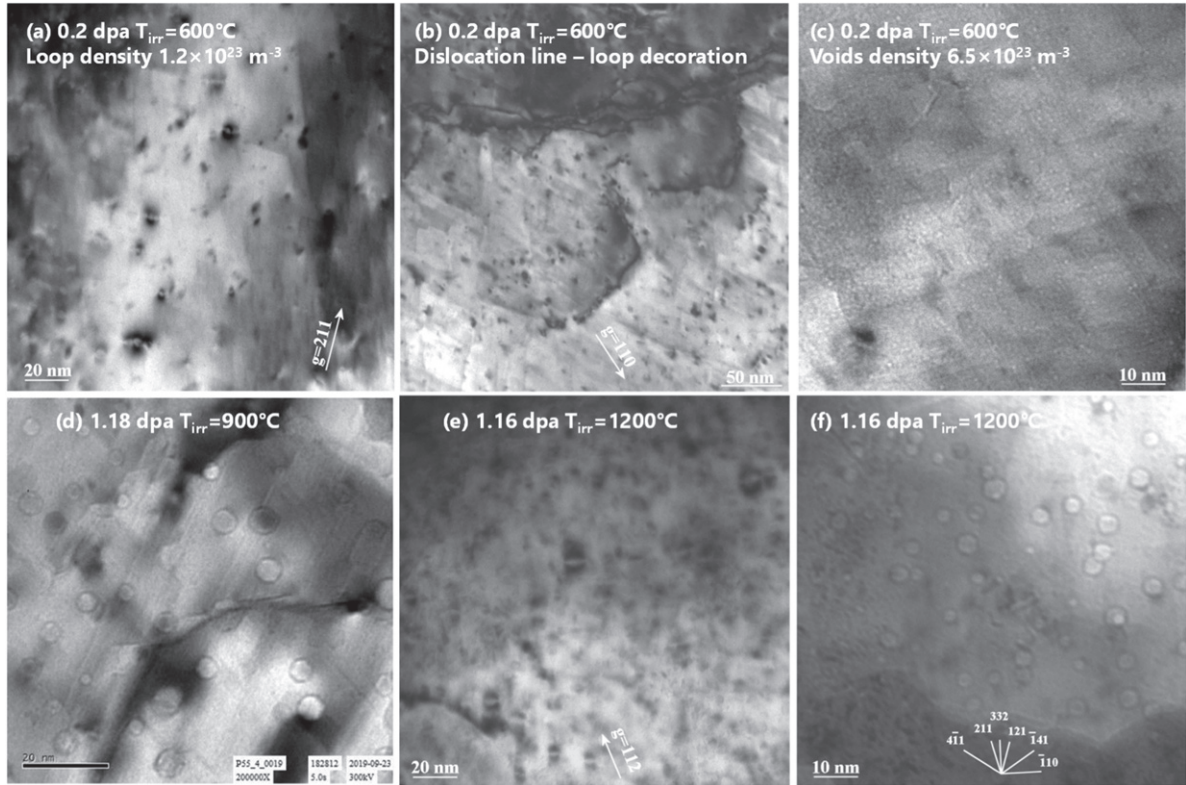

Figure 4. Examples of pure tungsten TEM images of the irradiation defects on the TEM lamellas extracted from the fracture toughness samples tested at 580 °C after 600 °C, 900 °C and 1200 °C irradiation. (*a*)–(*c*) show the microstructure of the 0.2 dpa irradiated sample, (*d*) 1.18 dpa sample, and (*e*), (*f*) 1.16 dpa sample.

deformation by the irradiation defects, which is in turn fully consistent with low values of the K_Q measured after 1−1.25 dpa irradiation in tests performed around 600 °C (see figure 2).

To shed a light on the type of the nano-structural defects induced by the irradiation damage in the fracture toughness samples, we provide a series of TEM micrographs (see figure 4) taken from the lamellas directly extracted from those samples (see schematics on figure 3). The microstructure of 0.2 dpa_600 °C irradiated sample is presented on the upper pane of figure 4. The irradiation did not have any remarkable impact on the sub-grain structure and dislocation line density.
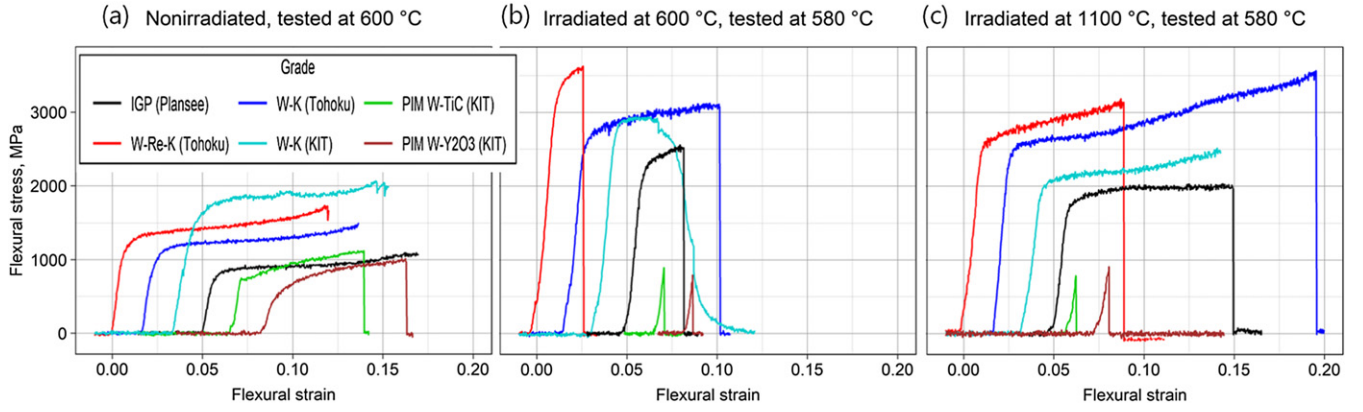
Figure 5. Comparison of 3 PB load-displacement curves obtained for the advanced W materials in (*a*) non-irradiated state; (*b*) irradiated at 600 °C at 1 dpa; (*d*) irradiated at 1100 °C at 1 dpa.
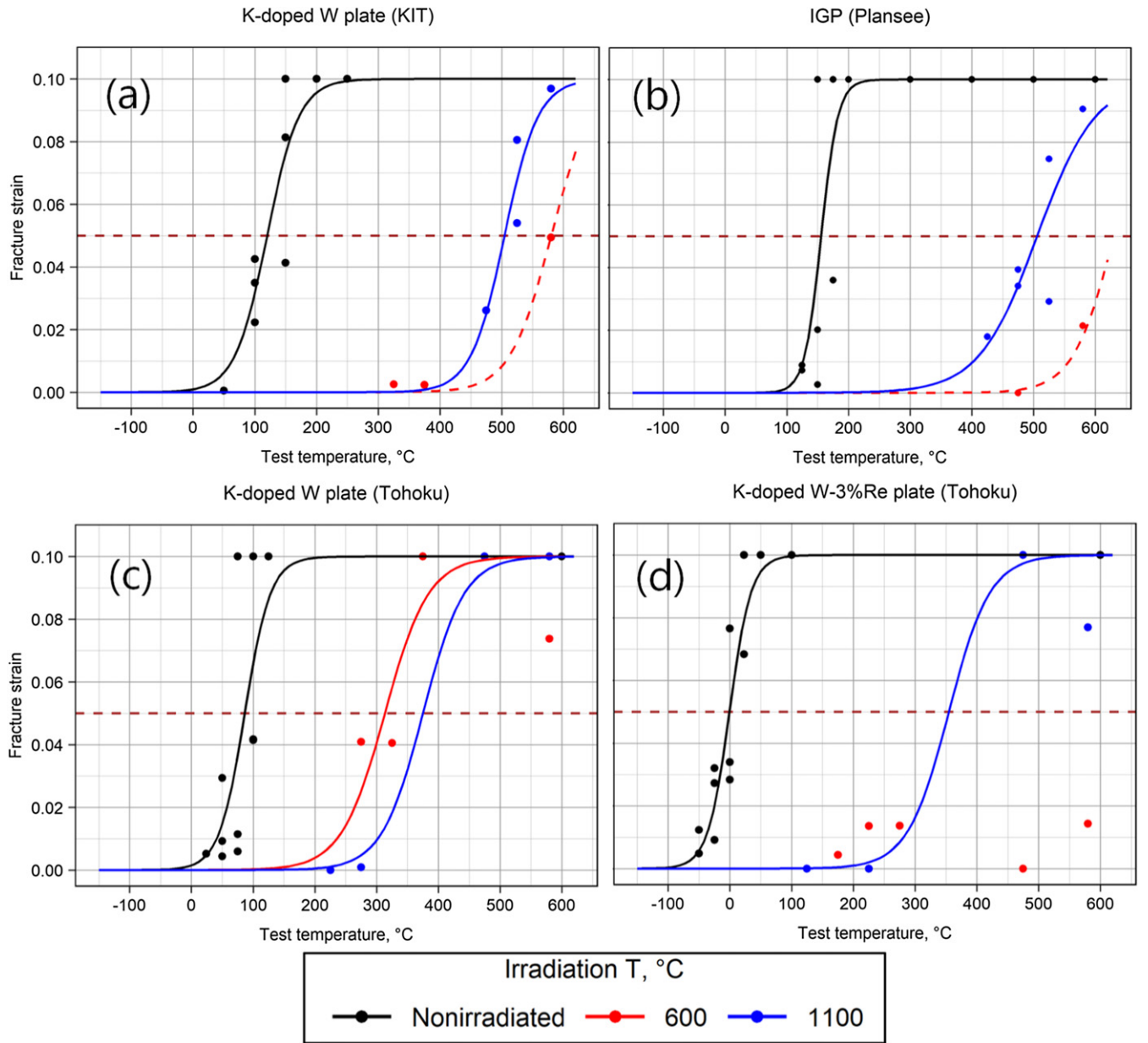

Figure 6. Derivation of DBTT using flexural strain at fracture values for (*a*) K-doped plate (KIT), (*b*) IGP (Plasee), (*c*) K-doped plate (Tohoku) and (*d*) K-doped W-3% Re plate (Tohoku) materials.

Table 2. DBBT (corresponding to 5% mean fracture strain) values obtained using equation (2) and *FS* data presented in figure 6.

Material	T_{DBTT} in non-irradiated state	T_{DBTT} at $T_{\mathrm{irr}} = 600\,°C$	T_{DBTT} at $T_{\mathrm{irr}} = 1100\,°C$
K-doped cold-rolled plate 1 mm (KIT), L-S orientation, figure 6(*a*)	150 ± 50 °C	∼600 °C, to be confirmed by high T tests	525 ± 75 °C
W bar (IGP) L-T orientation, figure 6(*b*)	150 ± 25 °C	>600 °C	550 ± 50 °C
K-doped rolled plate 7 mm (Tohoku), L-S orientation, figure 6(*c*)	75 ± 25 °C	325 ± 50 °C	325 ± 25 °C
K-doped 3 at.% Re-alloyed rolled plate 7 mm (Tohoku), L-S orientation, figure 6(*d*)	0 ± 25 °C	>600 °C	350 ± 100 °C

The newly formed defects were thus dislocation loops and voids. The majority of the loops are of $a/2\,\langle 111 \rangle$ type (fraction of $a\,\langle 100 \rangle$ loops is less than 5%). The loop density is $(1.2 \pm 0.3) \times 10^{23}\ \mathrm{m}^{-2}$ and the average size is 3.9 ± 1.1 nm, see example of the loop pattern on figure 4(*a*). Some dislocation lines appear to be strongly decorated by the loops as shown in figure 4(*b*). The voids are small (the mean size is (0.79 ± 0.11) nm) and numerous (the density is $6.5 \times 10^{23}/\mathrm{m}^3$), the corresponding TEM image is depicted in figure 4(*c*). Given the limited Re/Os transmutation at 0.2 dpa (0.4 at.% Re, 0.02 at.% Os), the presence of precipitates is not expected and was not identified by the applied TEM analysis. Also, the observed microstructure is in good agreement with the one found by Hasegawa *et al* under similar irradiation conditions (0.15–0.17 dpa, 600 °C–800 °C) [47, 48]. At high dpa/high irradiation temperature, the voids are much more pronounced, such that at 1.18 dpa_900 °C the void size ranges from few up to 15 nm with a mean value of 6 nm, figure 4(*d*). At 1200 °C, the mean size of voids is about 4 nm and the upper size reaches ∼10 nm. It is important to mention that dislocation loops are also present in the samples irradiated at 900 and 1200 °C (see figure 4(*e*)), however, their density is considerably lower than what is observed at 0.2 dpa_600 °C. The reduction of the loop density with the increase of the irradiation temperature above 800 °C is also fully consistent with the recent TEM studies applied to various neutron irradiated tungsten grades [46, 49]. As already noted above, the presence of non-coherent phases at the high irradiation temperature and ∼1 dpa damage level (e.g. see review of Rieth [11] and references cited therein) is to be expected. Revealing and characterizing these precipitates as well as possible segregation zones implies an advanced microstructural analysis using multiple TEM–EDX detectors and atom probe techniques, which is the next planned investigation step.

3.1.2. Advanced tungsten materials. The screening assessment of the irradiation effects in the advanced tungsten materials was performed using mini-bend samples. The primary objective was to clarify, which materials would remain ductile within the 600 °C threshold after the irradiation exposure up to ∼1 dpa at 600 and 1100 °C. The flexural stress–strain diagram for the non-irradiated materials is presented in figure 5(*a*), showing an example of the performance at 600 °C. The change of the response after the irradiation at 600 and 1100 °C is shown, respectively, in figures 5(*b*) and (*c*). The curves clearly
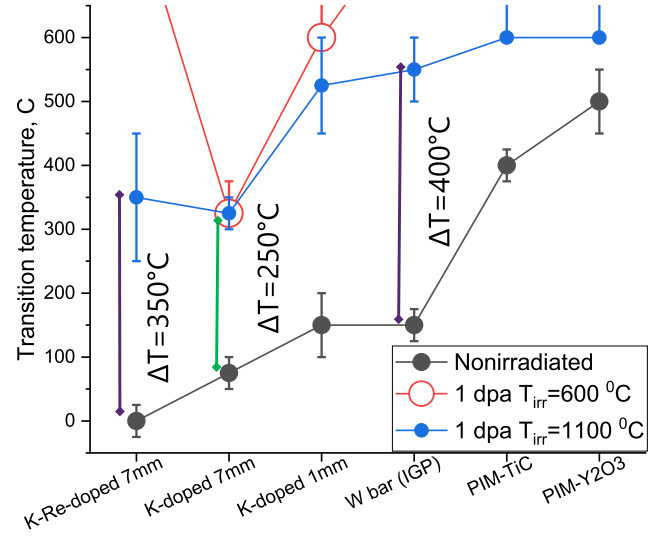
Figure 7. DBTT for the advanced and baseline W materials after irradiation at 600 and 1100 °C at 1 dpa.

show a significant irradiation hardening (i.e. increase of the stress level corresponding to the transition from elastic to plastic deformation) with still remaining ductility in all materials except the two PIM grades. Fracture of the PIM materials turned out to be fully brittle, also confirmed by SEM investigation, though not provided here. The amplitude of the irradiation hardening depends on the irradiation temperature and it is evidently lower for 1100 °C, for instance the apparent yield point (inflection form linear to plastic deformation) increases by a factor of two, which implies a similar increase of the tensile yield stress. The latter observation holds for most of the tested materials, but not for K-doped plate (W–K, KIT supplied). This material demonstrates a considerably lower irradiation-induced hardening, which might be linked with ultra-fine grain microstructure that renders high density of sinks sucking mobile irradiation defects. It is clear that the plate products (i.e. W–K and W–Re–K) as well as reference W bar (IGP) exhibit ductility at 580 °C after the irradiation at both temperatures. To determine the DBTT, bending tests were conducted at lower temperatures.

The DBTT criterion is adopted from [25]. T_{DBTT} is obtained by fitting the flexural strain at fracture (*FS*) vs test temperature through setting upper threshold strain (FS_{top}) as 10% and the
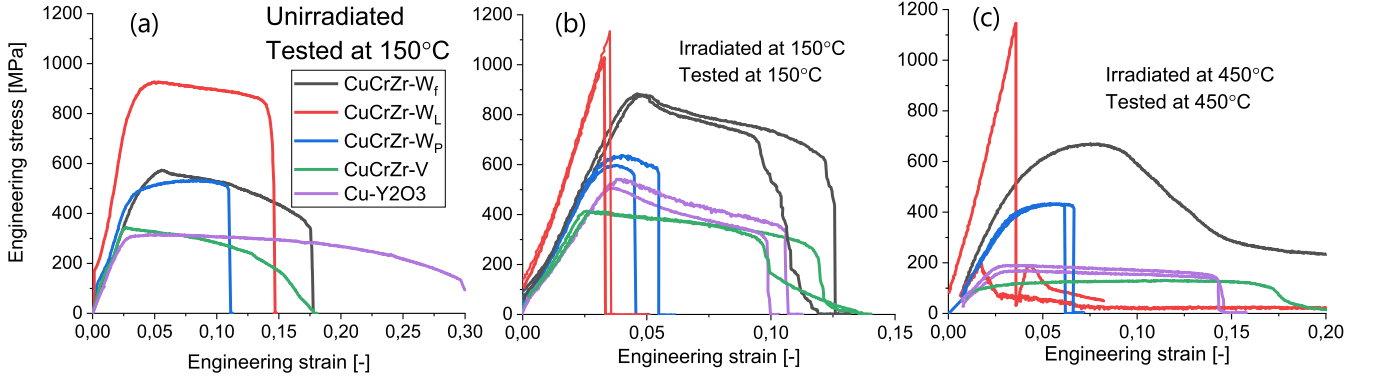
Figure 8. Engineering stress–strain curves for the advanced Cu alloys in (*a*) non-irradiated state tested at 150 °C; (*b*) irradiated and tested at 150 °C; (*c*) irradiated and tested at 450 °C.
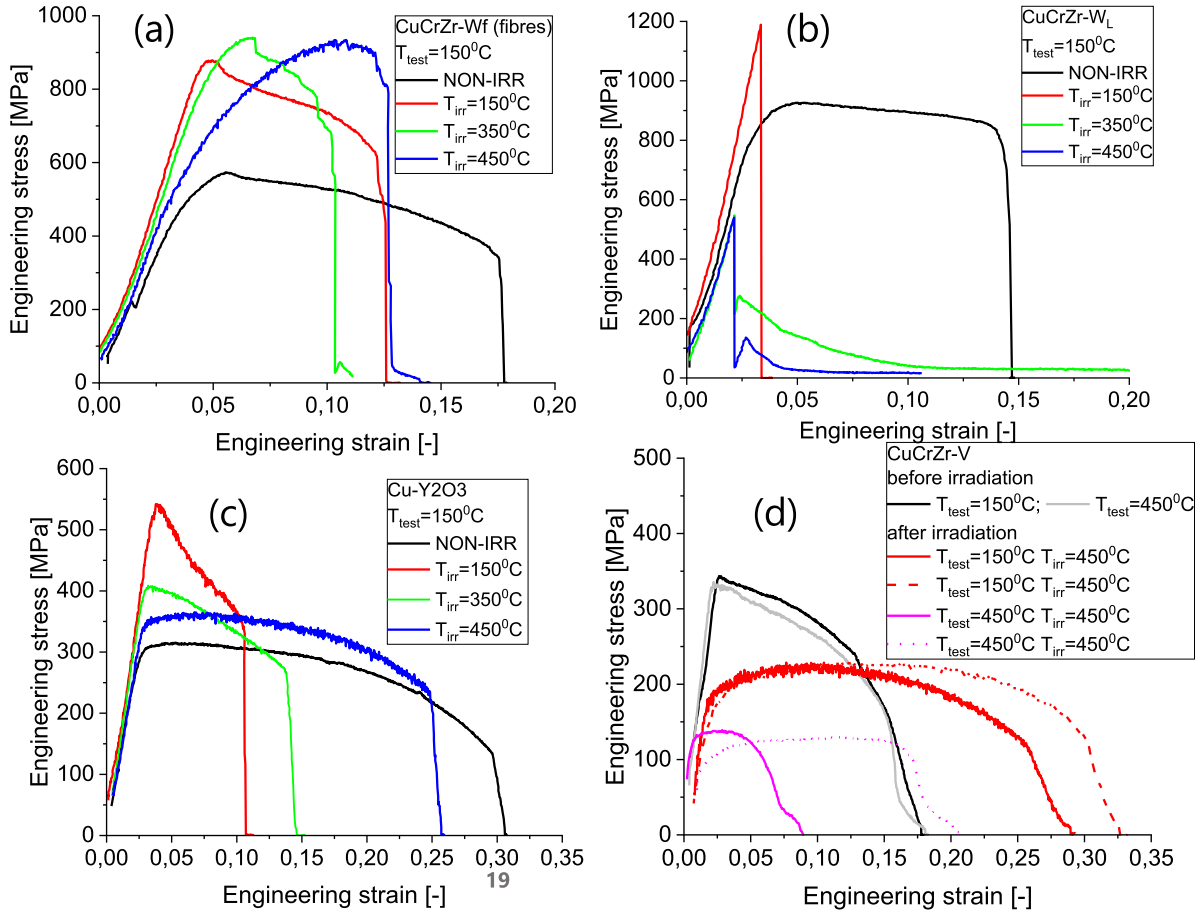

Figure 9. Engineering stress–strain curves for the advanced Cu alloys, namely: (*a*) CuCrZr–W$_f$, (*b*) CuCrZr–W$_L$, (*c*) Cu–Y$_2$O$_3$ and (*d*) CuCrZr–V. The irradiation and test temperatures are provided on the corresponding legends.

lower strain (FS_{base}) as 0%, with the equation:

$$FS(T) = \frac{10\%}{1 + \exp\left(C\left(T_{\text{DBTT}} - T\right)\right)}, \quad (2)$$

where C is the slope of the transition curve; T is the test temperature. In this case, T_{DBTT} corresponds to the mean strain at fracture being 5%, which is also the criterion proposed in [50]. Note that $FS(T)$ is the plastic flexural strain defined by subtracting the elastic strain from the load-displacement curve.

FS vs temperature is displayed in figure 6 for the cold-rolled 1 mm W plate (KIT), the reference W bar (IGP) and both 7 mm K-doped W and W/Re plate products. Given the upper test temperature of 580 °C, T_{DBTT} could not be determined for the PIM W grades (not shown on figure 6) the W–Re–K plate as well as the IGP W irradiated at 600 °C, as in all those cases it apparently lies above 600 °C.

Table 2 and figure 7 summarize the DBTT values and related error, which is defined as the temperature range where
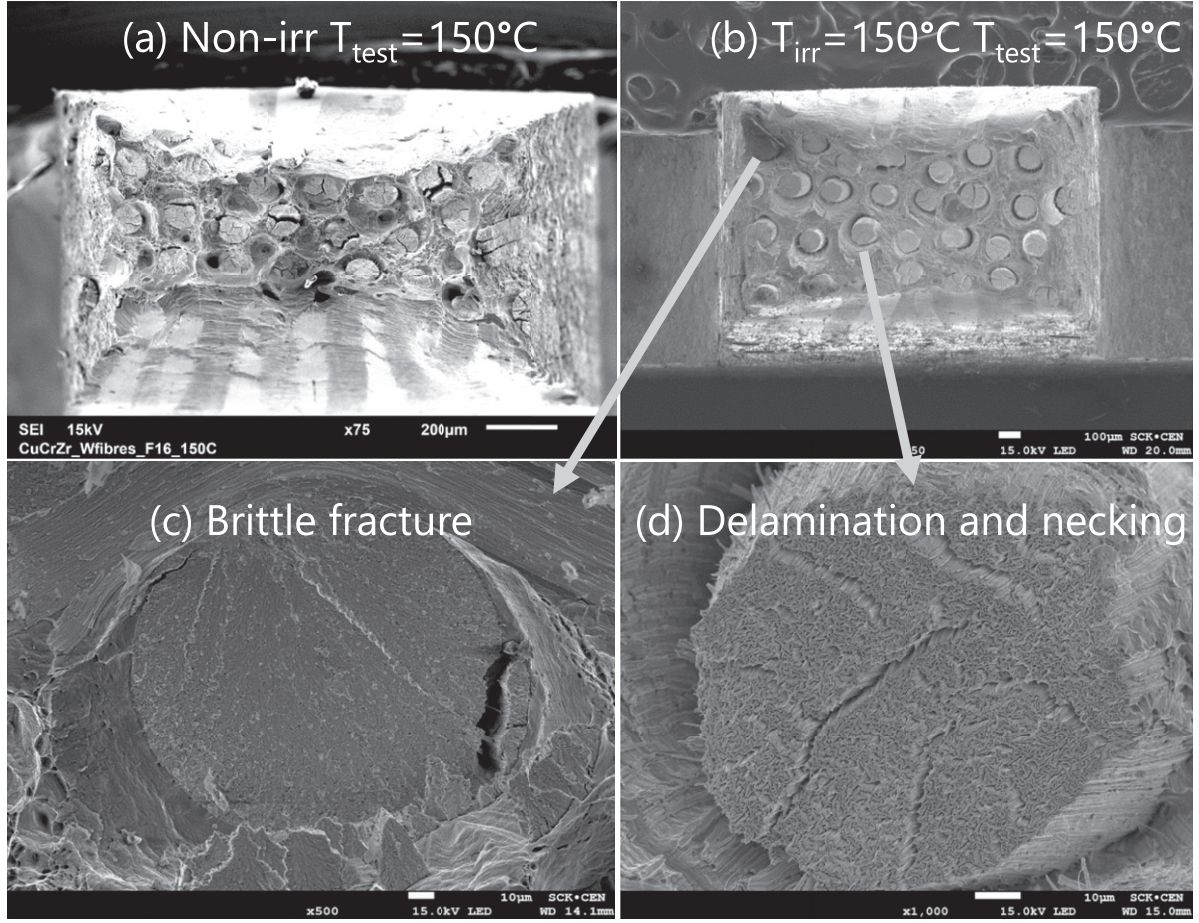
Figure 10. Fracture surface of the CuCrZr–W_f composites $T_{irr} = T_{test} = 150\,°C$. (*a*) and (*b*) show the overall view of the fracture surface of the reference and irradiated samples. (*c*) and (*d*) show zoomed microstructure of the ruptured wires which exhibited different fracture modes.

the plastic flexural strain at fracture exceeds 5% (hence, it depends on the density of points near the DBTT). Note that the bend samples were tested in L-T orientation, which is why T_{DBTT} (IGP) is much lower than the one determined for the T-L orientation in figure 2(*a*). Figure 7 reveals that ΔDBTT has a strong dependence on the irradiation temperature. The K-doped 7 mm plate exhibits the smallest DBTT shift of ~250 °C at both irradiation temperatures. The addition of 3 at.% Re yields to a considerable increase of the DBTT at $T_{irr} = 600\,°C$.

The detrimental effect of Re alloying on the DBTT shift might be explained taking into account the recent atom probe studies performed by Hwang *et al* [51], who investigated W and W-10Re samples irradiated at 0.9 dpa_550 °C–538 °C. In the latter work, the formation of high density of Re–Os–rich solute clusters was found by ATP, while these defects were irresolvable to TEM. The number density of those clusters was reaching a value of ~2 × 10^{24} m^{-3}, which is about two orders of magnitude higher than the density of the TEM-observed dislocation loops. In general, Hasegawa *et al* [47] have explained that the impact of the alloying with Re on the resulting microstructure depends on the irradiation temperature. At low irradiation temperatures, Re alloying suppresses the void lattice formation and alternates the accumulation of dislocation loops, while Re atoms retaining in solution

enhance ductility. At high irradiation temperature, the transmutation of Re into Os promotes premature formation of χ and σ phases leading to the massive phase decomposition which is detrimental for the mechanical performance.

The DBTT shift in the cold-rolled K-doped 1 mm plate is 375 °C, and it is 400 °C for the reference W bar at $T_{irr} = 1100\,°C$, while at $T_{irr} = 600\,°C$ both materials exhibit DBTT at or exceeding 600 °C, which needs in both cases further experimental clarification. Combining the results of the bending tests with the data presented in figure 2 for the reference W bar (IGP), one can assign a temperature range of 900 °C–1100 °C as the temperature range in which under irradiation conditions of 1 dpa and a Re generation rate of 2 at.%/dpa the DBTT of this material would still stay below this temperature. With this respect, the DBTT of K-doped 7 mm plate (Tohoku), irradiated at the same conditions as IGP, is only (325 ± 50) °C, which indicates a reduction of the lower bound for the acceptable operational temperature range under the given conditions to at least 600 °C.

3.2. Advanced copper-based materials

Presentation of the results obtained for the Cu-based materials will comprise the data obtained at the upper and lower boundary of the irradiation and test temperatures i.e. 150
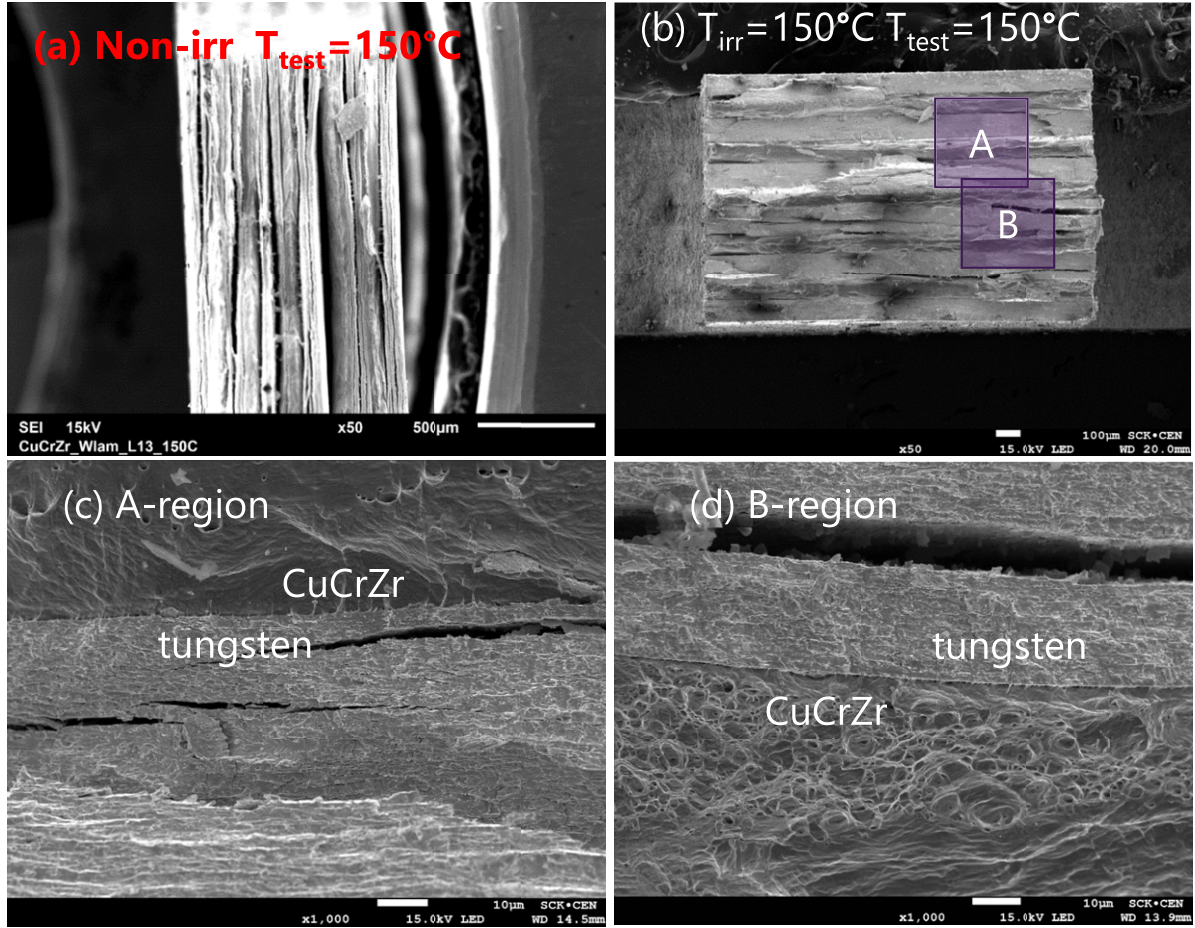
10

Figure 11. Fracture surface of the CuCrZr–W laminate composites $T_{irr} = T_{test} = 150\,°C$. (*a*) and (*b*) show the overall view of the fracture surface of the reference and irradiated samples. (*c*) and (*d*) show zoomed microstructure of the two regions near the W–CuCrZr layers.

and 450 °C, as this will allow assessing the extension of the low-temperature embrittlement and high temperature softening. Figure 8(*a*) shows the engineering stress-strain curves for the non-irradiated materials, figures 8(*b*) and (*c*) show these curves, at $T_{irr} = T_{test} = 150\,°C$ and $T_{irr} = T_{test} = 450\,°C$, respectively. The main observed irradiation induced effects are a reduction of total elongation seen for all tested materials at 150 °C, embrittlement observed for the Cu–W laminates, and strength reduction for the CuCrZr-V at 450 °C.

The stress–strain response at the test temperature of 150 °C is compared for CuCrZr–W_f, CuCrZr–W_1 and Cu-ODS materials in figures 9(a)–(c) for all three investigated irradiation temperatures. For the Cu–W_f, figure 9(*a*), the main effect of the irradiation is expressed in considerable irradiation hardening i.e. the rise of UTS by a factor of two and only moderate reduction of the elongation. By increasing the irradiation temperature from 150 °C up to 450 °C, the elongation partially recovers without any significant change in the UTS. Figure 10 provides SEM micrographs of the fracture surface of reference and 150 °C-irradiated samples, both tested at 150 °C. The specimens are characterized by less necking and a related lower reduction of area in the irradiated sample, i.e. compare figures 10(*a*) and (*b*). Close inspection of the tungsten fibers surface reveals that after the irradiation several fibers fractured in a brittle manner such as the one shown in figure 10(*c*). Other

fibers exhibit typical fracture pattern registered in the non-irradiated fibers tested individually at RT and elevated temperatures [52]. The surrounding copper matrix is deformed in a ductile mode by dimple rupture.

CuCrZr–W_L samples (see figure 9(*b*)) exhibit no ductile deformation when tested at 150 °C after the irradiation at 150, 350 or 450 °C. In fact, very similar results were found at other test temperature. The fracture surface of reference and 150 °C-irradiated samples tested at 150 °C are shown in figure 11. The fracture of the reference sample occurs by the delamination and necking of individual tungsten grains (fully in line with reference [33]), see figure 11(*a*), while the copper interlayers exhibit fracture by dimple rupture. After the irradiation, Cu-interlayers still show ductile deformation with well-resolved dimples, while W foils exhibit brittle intergranular fracture with large lateral cracks emerging near the W–Cu interfaces. Examples of such cracks are shown for two different fracture areas on figures 11(*c*) and (*d*). The irradiation embrittlement of Cu–W laminates has been already reported by Garrison *et al* [53], however, the irradiation was performed under conditions (HFIR, Rabbit) causing a higher Re/Os generation rate in tungsten, and higher irradiation temperatures (400 °C–800 °C) were explored. The present results confirm the irradiation embrittlement.
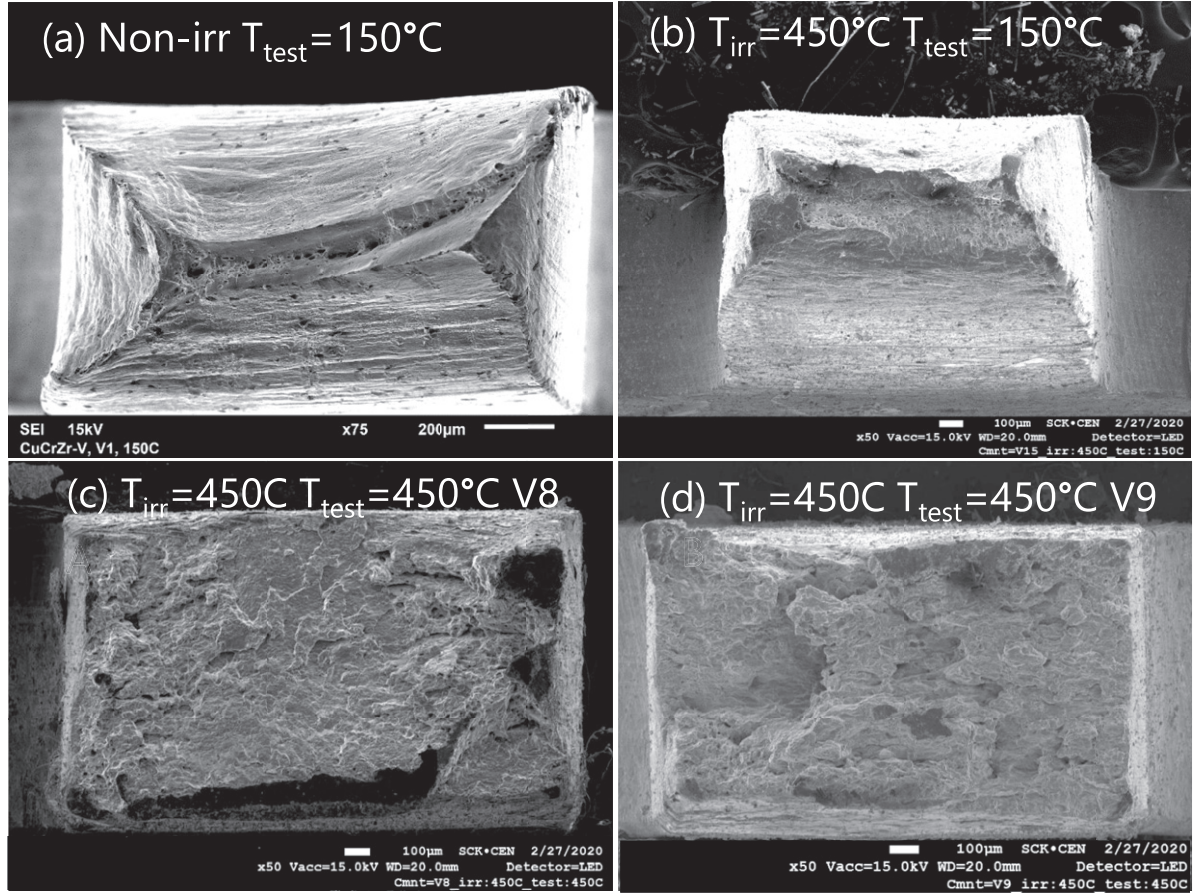
Figure 12. Fracture surface of the CuCrZr–V $T_{irr} = 450\,°C$ tested at 150 and 450 °C. (*a*) shows the microstructure of the non-irradiated sample tested at 150 °C. (*b*) shows the microstructure of the irradiated material tested at 150 °C. (*c*) and (*d*) show the microstructure of the irradiated material tested at 450 °C.

The Cu-ODS material (see figure 9(*c*)) exhibits at $T_{irr} = 150\,°C$ considerable hardening (UTS increase by 80%) and zero uniform elongation, although the post-necking elongation yields to 8%. Increasing the test temperature up to 450 °C leads to the progressive reduction of the UTS and recovery of the total and uniform elongation.

The tensile data for the V–CuCrZr are presented in figure 9(*d*), and there we focus on the response after the irradiation at 450 °C due to the apparent loss of strength and ductility. For reference, the response of the material in its non-irradiated state is also presented. After irradiation, the UTS drops from 350 MPa down to 130 MPa. The reduction of the test temperature to 150 °C leads to the UTS value of 220–230 MPa—being still much lower than the UTS in the non-irradiated state. Apparently, the 450 °C irradiation has modified the structure and/or size/density distribution of strengthening particles. Figure 12 provides SEM images of the fracture surface after testing at 150 and 450 °C. In the non-irradiated state, see figure 12(*a*), there is excessive post-necking deformation leading to nearly neck-to-edge fracture surface. The fracture occurs by dimple rupture and shear, and nearly the same deformation pattern is observed at 450 °C. The sample irradiated at 450 °C and tested at 150 °C also shows quite significant post-necking deformation, see figure 12(*b*), although the reduction area is smaller. The fracture mode remains the same as before

the irradiation i.e. dimple rupture. The tests performed at 450 °C yielded to practically no post-necking deformation, as is shown in figures 12(*c*) and (*d*) for the two samples whose stress–strain responses are provided in figure 9(*d*). Very low UTS as well as negligible post necking deformation at 450 °C is quite unexpected given a good ductility observed on the same set of samples at 150 °C.

4. Summary and outlook

The present contribution covers two major topics: (i) irradiation-induced embrittlement of pure W and advanced W alloys in a wide temperature range up to 1200 °C—corresponding to the surface temperature of divertor PFCs in the high flux region under steady-state operational conditions; (ii) strength and ductility of advanced Cu-alloys/composites under operational conditions in a water-cooled divertor scenario and exploring a possibility to extend the operational temperature window in the upper range from 300 °C–350 °C to 450 °C, otherwise limited by irradiation softening and creep taking place in the ITER baseline CuCrZr alloy.

A major step forward has been realized in terms of the assessment of the effect of neutron irradiation exposure on engineering-relevant mechanical properties (such as

fracture toughness) at high temperature at ∼1 dpa (W to Re transmutation rate of 2 at%/dpa). For the commercially pure baseline W, the threshold boundary for ductile operation lies in the range between 900 °C–1100 °C, as determined on the basis of fracture toughness and bending tests. Irradiation at lower temperatures leads to operational embrittlement i.e. fracture toughness decreases to the lower shelf value, no ductile deformation. Given the currently available knowledge from other irradiation campaigns, including Gd shielded irradiation, a severe embrittlement at high irradiation temperature found here is consistent with a large increase of the hardness found earlier.

Screening bending tests applied to a set of newly developed tungsten alloys/composites, also irradiated up to 1 dpa, have shown that some solutions (involving K-doping and rolling) truly demonstrate an enhanced tolerance to neutron irradiation exhibiting ductile behavior below 600 °C. Hence, the lower bound of the operational temperature window in which ductile performance up to 1 dpa has been registered might be reduced from (900–1100) °C to 600 °C. It would be important to assess the fracture toughness and tensile characteristics of those prospective grades under the same irradiation conditions as studied here. The optimum combination of the rolling, K-doping and Re-alloying as well as the eventual resistance/degradation of such K–Re–W grades under irradiation remains to be understood requesting the application of high-resolution microstructural techniques.

The assessment of the tensile properties of several advanced Cu-based alloys have also revealed some prospective solutions as well as brought unexpected outcomes. W_f- and W particle-reinforced materials sustained high tensile strength after the irradiation at 450 °C showing resistance against irradiation softening. CuCrZr–W_f composites have shown the irradiation hardening, however, W fibers sustain ductile deformation ability even at the lower limit test temperature conditions. Cu-ODS material has shown moderate irradiation hardening accompanied with the reduction of the total elongation. In the case of W-particle materials, the reduction of the uniform and even total elongation was considerable at each studied temperature. The originally promising CuCrZr–W laminates were found to exhibit brittle deformation at every combination of the irradiation/test condition studied. The irradiation softening and strong reduction of the reduction area has been revealed in the V-alloyed CuCrZr after irradiation at 450 °C, which has not been expected either.

To finalize, we bring an outlook for future studies which will require both fundamental understanding of irradiation damage as well as seeking for new technological solutions. An unexpected irradiation embrittlement of W–Cu laminates requires detailed microstructural investigation of the W–Cu interfaces as cracks were seen to initiate in the vicinity of those regions. Understanding the irradiation effect on the W–Cu interface is of general interest for the ITER PFCs. Currently, it is unclear whether the same severe damage would occur on the macroscopic W–Cu–CuCrZr joint. High resolution TEM and atom probe investigations are of high relevance for the V-alloyed CuCrZr, which revealed pronounced strength loss and

decrease of the reduction area after the irradiation and testing at 450 °C. Surprisingly, the elongation at 150 °C is much higher than at 450 °C, pointing at some interplay between the irradiation microstructure and plastic deformation mechanisms (e.g. thermally activated plastic deformation removes the irradiation defects causing the observed softening, possibly coupled with dislocation channelling). The performance of the Cu–W_f composites is found promising, yet the endurance of the W fibers under neutron exposure in terms of ductility exhaustion is a very important question to be answered for both W- and Cu-based composites.

With regard to the W grades, further optimization of the PIM fine-grain structured tungsten is needed to reduce the DBTT in the non-irradiated state. A good resistance against the irradiation embrittlement was revealed for the heavily rolled K-doped plates at 1 dpa and 2 at.% Re/dpa. However, depending on the specific location of tungsten, the transmutation rate and accumulation of Re and Os will differ. Alloying of W by Re (without applying neutron irradiation) demonstrates an improvement in terms of DBTT reduction without compromising high temperature performance [7]. However, the interplay of transmutation and irradiation damage accumulation as well as irradiation-induced secondary phase formation [46, 54] in the Re-added alloys needs to be investigated further. The two effects may counter-act each other depending on the irradiation temperature, fluence and spectrum, which would differ for the plasma-facing side of W block and the one behind the cooling pipe.

Acknowledgments

ORCID iDs

M. Rieth ⓘ https://orcid.org/0000-0002-6231-6241
G. Pintsuk ⓘ https://orcid.org/0000-0001-5552-5427
K. Mergia ⓘ https://orcid.org/0000-0002-2633-8750
M. Wirtz ⓘ https://orcid.org/0000-0002-1857-688X

References

[1] Litnovsky A. *et al* 2020 Smart tungsten-based alloys for a first wall of DEMO *Fusion Eng. Des.* **159** 111742
[2] Sheng H., Uytdenhouwen I., Van Oost G. and Vleugels J. 2012 Mechanical properties and microstructural characterizations of potassium doped tungsten *Nucl. Eng. Des.* **246** 198–202
[3] Battabyal M., Schaublin R., Spatig P. and Baluc N. 2012 W-2 wt.% Y$_2$O$_3$ composite: microstructure and mechanical properties *Mater. Sci. Eng.* A **538** 53–7
[4] Huang B., chen L., Qiu W., Yang X., Shi K., Lian Y., Liu X. and Tang J. 2019 Correlation between the microstructure,

mechanical/thermal properties, and thermal shock resistance of K-doped tungsten alloys *J. Nucl. Mater.* **520** 6–18

[5] Matsuo S., Kurishita H., Arakawa H., Takida T., Kato M., Yamamoto Y., Takebe K., Kawai M. and Yoshida N. 2008 Deformability enhancement in ultra-fine grained, Ar-contained W compacts by TiC additions up to 1.1% *Mater. Sci. Eng.* A **492** 475–80

[6] Nogami S., Hasegawa A., Fukuda M., Rieth M., Reiser J. and Pintsuk G. 2021 Mechanical properties of tungsten: recent research on modified tungsten materials in Japan *J. Nucl. Mater.* **543** 152506

[7] Nogami S., Hasegawa A., Fukuda M., Watanabe S., Reiser J. and Rieth M. 2020 Tungsten modified by potassium doping and rhenium addition for fusion reactor applications *Fusion Eng. Des.* **152** 111445

[8] Pintsuk G. and Uytdenhouwen I. 2010 Thermo-mechanical and thermal shock characterization of potassium doped tungsten *Int. J. Refract. Met. Hard Mater.* **28** 661–8

[9] Xie Z.M. *et al* 2015 Extraordinary high ductility/strength of the interface designed bulk W–ZrC alloy plate at relatively low temperature *Sci. Rep.* **5** 16014

[10] Pintsuk G., Diegele E., Dudarev S. L., Gorley M., Henry J., Reiser J. and Rieth M. 2019 European materials development: results and perspective *Fusion Eng. Des.* **146** 1300–7

[11] Rieth M., Doerner R., Hasegawa A., Ueda Y. and Wirtz M. 2019 Behavior of tungsten under irradiation and plasma interaction *J. Nucl. Mater.* **519** 334–68

[12] Barabash V., Federici G., Rödig M., Snead L.L. and Wu C.H. 2000 Neutron irradiation effects on plasma facing materials *J. Nucl. Mater.* **283–287** 138–46

[13] Barabash V.R., Kalinin G.M., Fabritsiev S.A. and Zinkle S.J. 2011 Specification of CuCrZr alloy properties after various thermo-mechanical treatments and design allowables including neutron irradiation effects *J. Nucl. Mater.* **417** 904–7

[14] You J.H. *et al* 2016 European DEMO divertor target: operational requirements and material–design interface *Nucl. Mater. Energy* **9** 171–6

[15] Pelowitz D. *et al* 2011 *MCNPX 2.7. 0 Extensions* Los Alamos National Laboratory

[16] Dudarev S.L. 2015 DPA definition and estimates (https://amdis.iaea.org/CRP/IrradiatedTungsten/RCM2/RCM2Presentation-DudarevDPA-2015-09-10.pdf)

[17] Stankovskiy A., Van den Eynde G. and Fiorito L. 2018 ALEPH V.2.7, a Monte Carlo burn-up code (SCK●CEN)

[18] Plompen A. *et al* 2017 JEFF-3.3 Nuclear Energrgy Agency

[19] Brown D.A. *et al* 2018 ENDF/B-VIII.0: the 8th major release of the nuclear reaction data library with CIELO-project cross sections, new standards and thermal scattering data *Nucl. Data Sheets* **148** 1–142

[20] Konobeyev A.Y., Fischer U., Korovin Y.A. and Simakov S.P. 2017 Evaluation of effective threshold displacement energies and other data required for the calculation of advanced atomic displacement cross-sections *Nucl. Energy Technol.* **3** 169–75

[21] Norgett M.J., Robinson M.T. and Torrens I.M. 1975 A proposed method of calculating displacement dose rates *Nucl. Eng. Des.* **33** 50–4

[22] Terentyev D., Chang C.-C., Yin C., Zinovev A. and He X.-F. 2021 Neutron irradiation effects on mechanical properties of ITER specification tungsten *Tungsten* **3** 415–33

[23] Nogami S., Terentyev D., Zinovev A., Yin C., Rieth M., Pintsuk G. and Hasegawa A. 2021 Neutron irradiation tolerance of potassium-doped and rhenium-alloyed tungsten *J. Nucl. Mater.* **553** 153009

[24] Gaganidze E., Chauhan A., Schneider H.-C., Terentyev D., Borghmans G. and Aktaa J. 2021 Fracture-mechanical properties of neutron irradiated ITER specification tungsten *J. Nucl. Mater.* **547** 152761

[25] Yin C., Terentyev D., Pardoen T., Petrov R. and Tong Z. 2019 Ductile to brittle transition in ITER specification tungsten

[26] Yin C. *et al* 2018 Tensile properties of baseline and advanced tungsten grades for fusion applications *Int. J. Refract. Met. Hard Mater.* **75** 153–62

[27] ASTM 2014 Standard test methods for bend testing of material for ductility E290-14 (ASTM International)

[28] ASTM 2012 Standard test method for linear-elastic plane strain fracture toughness KIC of metallic materials E399-12 (ASTM International)

[29] Terentyev D., Riesch J., Dubinko A., Khvan T. and Zhurkin E.E. 2019 Fracture surfaces of tungsten wires used in fiber-reinforced plasma facing components: effect of potassium doping and high temperature annealing *Fusion Eng. Des.* **146** 991–4

[30] Wirtz M., Linke J., Loewenhoff T., Pintsuk G. and Uytdenhouwen I. 2016 Thermal shock tests to qualify different tungsten grades as plasma facing material *Phys. Scr.* **T167** 014015

[31] Antusch S. *et al* 2015 Mechanical and microstructural investigations of tungsten and doped tungsten materials produced via powder injection molding *Nucl. Mater. Energy* **3–4** 22–31

[32] Reiser J., Wurster S., Hoffmann J., Bonk S., Bonnekoh C., Kiener D., Pippan R., Hoffmann A. and Rieth M. 2016 Ductilisation of tungsten (W) through cold-rolling: R-curve behaviour *Int. J. Refract. Met. Hard Mater.* **58** 22–33

[33] Reiser J. *et al* 2017 Ductilisation of tungsten (W): tungsten laminated composites *Int. J. Refract. Met. Hard Mater.* **69** 66–109

[34] Reiser J., Rieth M., Möslang A., Dafferner B., Hoffmann A., Yi X. and Armstrong D.E.J. 2013 Tungsten foil laminate for structural divertor applications—tensile test properties of tungsten foil *J. Nucl. Mater.* **434** 357–66

[35] Muller A.V., Boswirth B., Cerri V., Greuner H., Neu R., Siefken U., Visca E. and You J.H. 2020 Application of tungsten–copper composite heat sink materials to plasma-facing component mock-ups *Phys. Scr.* **T171** 014015

[36] Von Muller A., Ewert D., Galatanu A., Milwich M., Neu R., Pastor J.Y., Siefken U., Tejado E. and You J.H. 2017 Melt infiltrated tungsten–copper composites as advanced heat sink materials for plasma facing components of future nuclear fusion devices *Fusion Eng. Des.* **124** 455–9

[37] Coenen J.W. *et al* 2019 Materials development for new high heat-flux component mock-ups for DEMO *Fusion Eng. Des.* **146** 1431–6

[38] You J.-H., Brendel A., Nawka S., Schubert T. and Kieback B. 2013 Thermal and mechanical properties of infiltrated W/CuCrZr composite materials for functionally graded heat sink application *J. Nucl. Mater.* **438** 1–6

[39] Gludovatz B., Wurster S., Hoffmann A. and Pippan R. 2010 Fracture toughness of polycrystalline tungsten alloys *Int. J. Refract. Met. Hard Mater.* **28** 674–8

[40] Faleschini M., Kreuzer H., Kiener D. and Pippan R. 2007 Fracture toughness investigations of tungsten alloys and SPD tungsten alloys *J. Nucl. Mater.* **367–370** 800–5

[41] Gaganidze E., Rupp D. and Aktaa J. 2014 Fracture behaviour of polycrystalline tungsten *J. Nucl. Mater.* **446** 240–5

[42] Garrison L.M. *et al* 2019 PHENIX U.S.-Japan collaboration investigation of thermal and mechanical properties of thermal neutron-shielded irradiated tungsten *Fusion Sci. Technol.* **75** 499–509

[43] Hu X., Koyanagi T., Fukuda M., Kumar N.A.P.K., Snead L.L., Wirth B.D. and Katoh Y. 2016 Irradiation hardening of pure tungsten exposed to neutron irradiation *J. Nucl. Mater.* **480** 235–43

[44] Koyanagi T., Kumar N.A.P.K., Hwang T., Garrison L.M., Hu X., Snead L.L. and Katoh Y. 2017 Microstructural evolution of pure tungsten neutron irradiated with a mixed energy spectrum *J. Nucl. Mater.* **490** 66–74

[45] Duerrschnabel M., Klimenkov M., Jaentsch U., Rieth M., Schneider H.C. and Terentyev D. 2021 New insights into microstructure of neutron-irradiated tungsten *Sci. Rep.* **11** 7572

[46] Klimenkov M., Jäntsch U., Rieth M., Schneider H.C., Armstrong D.E.J., Gibson J. and Roberts S.G. 2016 Effect of neutron irradiation on the microstructure of tungsten *Nucl. Mater. Energy* **9** 480–3

[47] Hasegawa A., Fukuda M., Yabuuchi K. and Nogami S. 2016 Neutron irradiation effects on the microstructural development of tungsten and tungsten alloys *J. Nucl. Mater.* **471** 175–83

[48] Hasegawa A., Fukuda M., Tanno T. and Nogami S. 2013 Neutron irradiation behavior of tungsten *Mater. Trans.* **54** 466–71

[49] Terentyev D., Yin C., Dubinko A., Chang C.C. and You J.H. 2021 Neutron irradiation hardening across ITER diverter tungsten armor *Int. J. Refract. Met. Hard Mater.* **95** 105437

[50] Lassila D.H., Magness F. and Freeman D. 1991 Ductile-brittle transition temperature testing of tungsten using the three-point bend test *Report UCRL-ID-108258* Lawrence Livermore National Laboratory

[51] Hwang T. *et al* 2018 Effect of neutron irradiation on rhenium cluster formation in tungsten and tungsten-rhenium alloys *J. Nucl. Mater.* **507** 78–86

[52] Terentyev D. *et al* 2019 Correlation of microstructural and mechanical properties of K-doped tungsten fibers used as reinforcement of tungsten matrix for high temperature applications *Int. J. Refract. Met. Hard Mater.* **79** 204–16

[53] Garrison L.M., Katoh Y., Snead L.L., Byun T.S., Reiser J. and Rieth M. 2016 Irradiation effects in tungsten-copper laminate composite *J. Nucl. Mater.* **481** 134–46

[54] Hu X., Parish C.M., Wang K., Koyanagi T., Eftink B.P. and Katoh Y. 2019 Transmutation-induced precipitation in tungsten irradiated with a mixed energy neutron spectrum *Acta Mater.* **165** 51–61